# A Novel DEM Extraction Method Based on Chain Correlation of CSAR Subaperture Images

Yishi Li, Leping Chen, Daoxiang An, and Zhimin Zhou

***Abstract*—Circular synthetic sperture radar (CSAR) can observe the target in 360° and obtain the target's total scattering information. By dividing the CSAR imaging data into subapertures, the target digital elevation model (DEM) information can be directly obtained. Aiming at the problems existing in the division and selection of subapertures when acquiring DEM, this article proposes a chain correlation method. First, the echo data of the full aperture is divided into multiple subapertures; then, the correlation between the two adjacent subapertures is used to perform correlation processing on the subaperture image, and then the DEM information is obtained. The chain correlation method proposed in this article takes advantage of the stronger correlation between adjacent subapertures, improves the accuracy of the algorithm, and effectively improves the overall efficiency of the algorithm. Finally, the effectiveness and reliability of the proposed method is verified by different measured data, and it is the first time our own collected Ku-band experimental data are used.**

***Index Terms*—Chain correlation, circular synthetic aperture radar (CSAR), digital elevation model (DEM), subaperture.**

## I. Introduction

SYNTHETIC aperture radar (SAR) imaging technology, as an important high-resolution earth observation technology method [1], has the characteristics of all-weather and all-day compared with optical radar. Circular SAR (CSAR) is a new SAR imaging mode, which has been rapidly developed and widely concerned in recent years. Compared with the traditional linear SAR (LSAR) mode, CSAR imaging forms a 360° synthetic aperture around the observation scene, with high resolution, 3-D reconstruction capabilities and omnidirectional multiangle observation capabilities [2].

In the 1990s, the concept of CSAR imaging was first proposed, and because of its unique advantages, it quickly became a research hotspot in SAR field [3]–[9]. During this period, University of Washington first analyzed and deduced the generalized ambiguity function of CSAR [1], and obtained the theoretical expressions of CSAR high resolution and planar resolution, which theoretically proved that CSAR has the potential of 3-D high-resolution imaging [10]. In the past ten years or so, with the continuous deepening of research, the unique advantages of CSAR imaging technology have become increasingly prominent, and have received widespread attention at home and abroad. US Air Force Research Laboratory (AFRL), French Aerospace Agency (FAA, ONERA) and other foreign institutions [11], National University of Defense Technology [12], Institute of Electrics, Chinese Academy of Sciences [13], Xidian University [14], and other high-level research institutions have all carried out relevant technical research. The research content mainly includes CSAR imaging mechanism, resolution analysis, imaging methods, motion compensation methods, and 3-D imaging.

In terms of CSAR 3-D information acquisition, the FAA used the SETHI airborne SAR system to carry out an X-Band CSAR test in Nimes, France in 2007 [15]–[17]. Based on the radar stereo measurement technology, the digital elevation model (DEM) of the building area in the observation scene is obtained through CSAR image parameter inversion. It highlights the potential of CSAR in topographic surveying and mapping, and proves that CSAR has incomparable advantages over linear SAR.

German Aerospace Center (Deutsches Zentrum für Luft- und Raumfahrt, DLR) carried out research on CSAR holographic imaging technology [18]–[21], and carried out a multibaseline fully polarized CSAR airborne test in Vordemwald, Switzerland, and obtained 3-D tomographic images of the observation scene. Then, the L-band fully polarized CSAR holographic tomography airborne test was carried out in Kaufbeuren, Germany, and a 3-D view of a holographic tomographic image of a certain forest area was obtained, which presented the original forest scene with high accuracy. The results show that CSAR holographic tomography technology has great potential in image interpretation applications such as scene 3-D reconstruction, forest crop management, and vegetation monitoring.

The Institute of Electronics, Chinese Academy of Sciences (IECAS) proposed a method of dividing the arc trajectory into multiple arcs in the CSAR mode, and using the similarity between subaperture images to directly obtain the DEM [22]. However, this method has only been experimentally verified in a microwave anechoic chamber and lacks the verification of the actual scene.

Mersin University in Turkey carried out a wide-area CSAR imaging experiment to study the imaging rules of the target at different imaging heights [23]. The results showed that when the target is at the imaging height, the target imaging focus is

Manuscript received January 21, 2021; revised April 27, 2021; accepted June 1, 2021. Date of publication June 11, 2021; date of current version September 10, 2021. This work was supported in part by the Natural Science Foundation of Hunan Province under Grant 2020JJ5661 and in part by the National Natural Science Foundation of China under Grant 61571447. *(Corresponding author: Leping Chen.)*

The authors are with the College of Electronic Science and Technology, National University of Defense Technology, Changsha 410073, China (e-mail: liyishilittleboy@163.com; gfkdclp@126.com; daoxiangan@nudt.edu.cn; zhouzhiminmail@163.com).

Digital Object Identifier 10.1109/JSTARS.2021.3088691

good, and when the target is not on the imaging plane, the target imaging appears scattered.

In the use of CSAR mode for 3-D imaging, National University of Defense Technology conducted experiments on extracting target contour information from CSAR 2D images and reconstructing target 3D images based on Gotcha data published by the US Air Force Research Laboratory (AFRL), [24]. In the 3D reconstruction results, the contour information of the target vehicle was clear. The 3-D image obtained is of high quality, and the vehicle size is estimated with high accuracy. Experimental results show that CSAR has great potential in 3D image reconstruction, target classification, and recognition applications.

Xidian University carried out a DEM extraction experiment of scene targets based on the Gotcha CSAR data published by AFRL [25]. Using the correlation between CSAR subaperture images, the joint correlation method was used to achieve an accuracy of 0.5 m to extract the DEM of observation scene targets. However, this method requires a lot of calculations and has a limited accuracy.

Stephan Palm proposed a framework to generate 3D point clouds by very high-resolution single-pass and single-channel CSAR [26], [27]. It can accurately determine very small and separated objects in 3D, as well as large buildings in complex urban scenes. The height of objects down to a size of 3-cm edge length could be determined with a height accuracy of $<$20 cm. However, it requires, in the W-Band, and a special aspect interval. The objects' 3D information of this precision could be extracted.

Based on the CSAR model to extract DEM information, the literature [22] divides the entire circle data into multiple arcs and calculates the correlation between each subaperture in the arc and the central subaperture to extract the target height information. This method only deals with the subaperture and central subaperture of each arc. The relevant information between other noncentral subapertures is not used, and the correlation between the subapertures is related to the azimuth angle between the subapertures. When the correlation between the subapertures in the arc is added and averaged, it will be affected by the lower correlation part. Combined with the verification of measured data, this method has low accuracy and poor effect on DEM extraction [25]. The joint correlation method used in literature [25], on the basis of literature [22], uses the relevant information between all subapertures in each arc, and calculates all subapertures in each arc. Finally, the DEM coefficients extracted from each arc are fused to obtain the DEM information of the whole scene. From the results, the DEM extraction accuracy of the method used in [25] has been improved, but this method generates too much calculation when calculating the correlation of all subapertures in each arc. There is a large amount of overlap between the arcs, resulting in a large number of recalculations for the relevant information between the subaperture images; and as the azimuth angle difference between the subapertures increases, the correlation between the subapertures will also decrease [22], which will incorporate more less relevant data, affecting the overall results.

To solve the above problems, this article proposes a chain correlation method, which divides the entire circle into nonoverlapping subapertures, gives the criteria for subaperture division. Then according to the algorithm, the adjacent subaperture images are calculated one by one. Finally, the DEM information obtained is added and averaged for fusion to obtain the DEM information of the whole scene. The algorithm proposed in this article makes full and reasonable use of relevant information between subapertures. It is presented in a 3-D diagram.

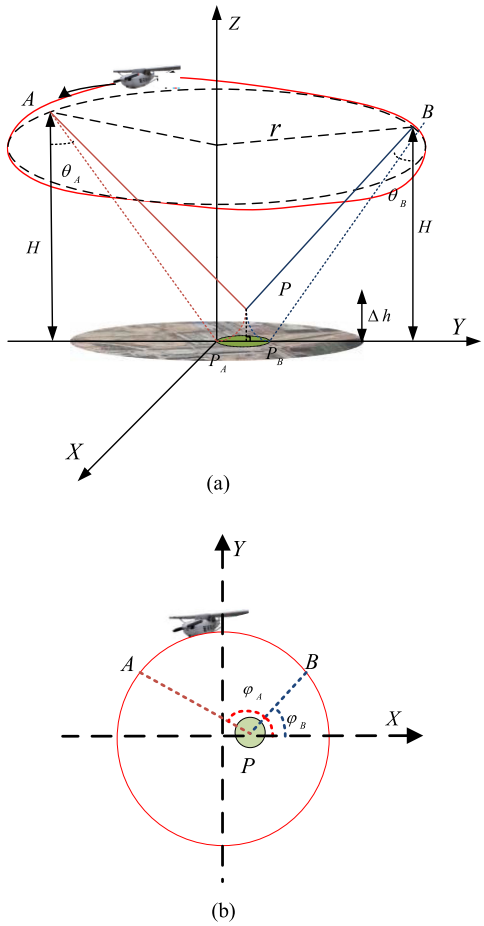


Fig. 1. CSAR mode imaging geometry. (a) Perspective. (b) Top view.

This article is arranged as follows. In Section II, the principle of extracting DEM information from CSAR model is analyzed. In Section III, the relevant steps of extracting DEM information by chain correlation method has been discussed. In Section IV, the two sets of measured data are compared and verified to prove the feasibility, effectiveness, and applicability of the algorithm.

## II. Characteristics Between Subapertures of CSAR for DEM Extraction

The schematic diagram of imaging geometry of the CSAR mode is shown in Fig. 1. The ground is the imaging plane, and the spatial rectangular coordinate system *XYZ* is constructed. The radar platform moves in a circular motion on a certain height plane. Determine the azimuth width of the subaperture according to the resolution requirement. Then divide the entire circle echo data into multiple subapertures of the same width. Through the back projection (BP) algorithm, the focus imaging processing is

performed on the echo data of each subaperture, and the CSAR subaperture image sequence is obtained.

From Fig. 1, there is a height difference between the imaging height and the true height of the target. This will cause the geometric deformation of the subaperture image [17]. The offset of the subaperture in the plane position and its actual position [25] is given by

$$\begin{cases} \Delta x_A = \Delta h \dfrac{\cos \varphi_A}{\tan \theta_A} \\ \Delta y_A = \Delta h \dfrac{\sin \varphi_A}{\tan \theta_A} \end{cases} \tag{1}$$

where $\varphi_A$ is the azimuth angle of the subaperture $A$ , is the lower viewing angle of the subaperture $A$ , and $\Delta h$ is the height difference between the imaging height and the true height of the target $P$. It can be seen that the geometric deformation of the subaperture is related to the difference between the actual elevation of the target and the elevation of the imaging plane. The greater the difference between the height, the greater the geometric deformation of the subaperture. At the same time, the incidence angle of wave $\theta$ and azimuth $\varphi$ of the radar platform will also affect the geometric deformation of the subaperture image. For the imaging plane of target $P$ on subaperture $B$ relative to its position offset on subaperture $A$ [25] is

$$\begin{cases} \Delta x_B - \Delta x_A = \Delta h \left[ \dfrac{\cos \varphi_B}{\tan \theta_B} - \dfrac{\cos \varphi_A}{\tan \theta_A} \right] \\ \Delta y_B - \Delta y_A = \Delta h \left[ \dfrac{\sin \varphi_B}{\tan \theta_B} - \dfrac{\sin \varphi_A}{\tan \theta_A} \right] \end{cases} \tag{2}$$

where $\varphi_B$ is the azimuth angle of the subaperture$B$ , $\theta_B$ is the lower viewing angle of the subaperture $B$ , $\Delta x_B$ is the horizontal offset of the subaperture $B$ in the plane position and its actual position, and $\Delta y_B$ is the corresponding vertical offset. It can be seen that the geometric deformation between the subaperture images is related to the difference in azimuth angle between the subapertures. The larger the azimuth angle between the subapertures, the greater the geometric deformation between the subapertures. At the same time, the correlation between subaperture images will also decrease as the azimuth angle between subapertures increases [22]. Next the experimental data (gotcha volumetric SAR data set, Version 1.0) released by the AFRL is used to verify this conclusion.

For a certain same azimuth angle difference, two subaperture images are selected at random, and the correlation coefficient between subaperture images is calculated in the following two ways: In the whole image and pixel by pixel. The difference of the subaperture azimuth angle ranges from 3° to 87°. To be consistent with the literature [25], for each azimuth angle difference, 10 pairs of subapertures are selected. The formula for correlation calculation is

$$C = \frac{D_A \cdot D_B}{\sqrt{{D_A}^2 \cdot {D_B}^2}} \tag{3}$$

where $D_A$ and $D_B$ are the image data of two adjacent subapertures, and $C$ is the correlation coefficient.

The standard deviation of each group of experimental results is calculated and the large bias value (the standard deviation is less than 0.15) is removed to reduce the influence of the bias value. The average value of these 10 pairs of subaperture image correlation coefficients is used as the subaperture image correlation coefficient of the difference in azimuth angles. Repeat the above experiment to get the experimental results of all azimuth angle difference. The result is shown in Fig. 2.

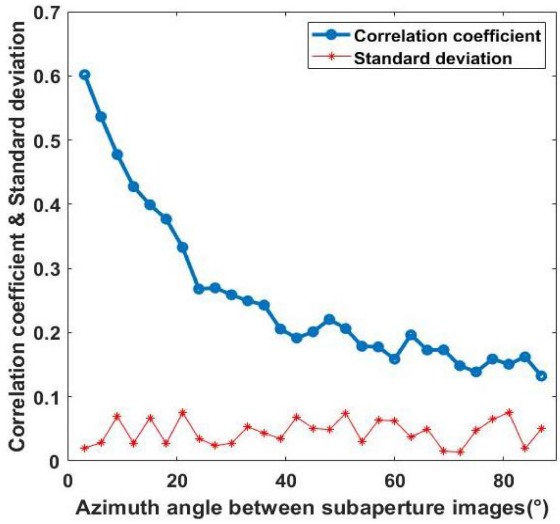


Fig. 2. Correlation between subaperture images varies with azimuth angle difference (blue line) and standard deviation of the results (red line).

It can be seen that the overall trend is monotonically decreasing. The correlation coefficient between the subaperture images decreases with the increase of the difference of the azimuth angle when the subaperture azimuth angle difference is from 3° to 43°. When it is 43°–87°, although the correlation changes slightly fluctuate, the overall correlation coefficient is generally too low, lower than 0.25, which will affect the DEM extraction accuracy [17].

For pixel-by-pixel estimation of the correlation coefficient, the formula for correlation calculation is as follows:

$$Q_m = \frac{[S_A(i,j) - \mu_A] \cdot [S_B(i,j) - \mu_B]}{\sqrt{[[S_A(i,j) - \mu_A]]^2 \cdot [S_B(i,j) - \mu_B]^2}} \tag{4}$$

$$Q = \frac{1}{M} \sum_{m=1}^{M} Q_m \tag{5}$$

where $S_A(i,j)$ and $S_B(i,j)$ are the image data in two adjacent subaperture sliders, $\mu_A$ and $\mu_B$ are the average values of data $S_A$ and $S_B$ in the sliders. The size of the slider is selected as $15 \times 15$ [25], $i, j \in [1, 15]$. Let $Q_m$ be the result of the correlation coefficient of the middle element in the slider. After traversing the entire subaperture image, the correlation coefficients of all pixels are accumulated and averaged. The obtained result $Q$ is the pixel-by-pixel correlation coefficient of two adjacent subaperture images.

According to the traditional method, when the difference in azimuth angles between subapertures varies from 3° to 42°, the correlation coefficient between the subaperture images decreases with the increase of the difference in azimuth angles. This provides a basis for the selection of subaperture division and azimuth angle.

## III. Chain Related DEM Extraction Method

In dividing the circle data into subapertures to extract DEM information, the original method does not make full and reasonable use of the correlation between subapertures. The joint correlation method used in [25] calculates the correlation of all subapertures in each arc, the calculation amount is too large, and the correlation between the subapertures with a larger azimuth angle is low [22]. The integration of this part of the data will reduce the accuracy of the results. When dividing arcs, there is a large amount of overlap between the arcs, resulting in a large number of repetitive calculations for the relevant information between the subaperture images, which makes the efficiency of the algorithm very slow.

To solve the above problems, this article proposes a chain-related processing method, which makes the DEM extraction result more accurate and more efficient. In order to obtain the DEM information of the target scene, using the 360° omnidirectional and multiangle observation capability of the CSAR mode, the circle trajectory of the entire radar platform is divided into multiple subapertures with the same arc length. First, use BP algorithm to image each subaperture data to obtain multiple subaperture images. Second, project each subaperture to its height direction, and each subaperture obtains imaging data of different imaging heights. Third, perform correlation calculations on two adjacent subapertures pixel by pixel to obtain DEM information of different azimuths. The DEM information of all azimuth angles is integrated to obtain all-round DEM information of the imaging area. Fig. 3 gives the flowchart of the proposed method.

The specific analysis of DEM extraction method is as follows.

### A. Step 1: Data Division

From Section II that the correlation between subaperture images is related to the azimuth angle between subaperture images, and the strength of the correlation between subaperture images will also affect the accuracy of extracting DEM information. The larger the azimuth angle between the subapertures, the weaker the correlation between the subaperture images, and the excessive position offset between the images will reduce the accuracy of the DEM information extraction. To ensure the accuracy of the results, the correlation coefficient between subapertures cannot be lower than 0.5 [17].

When the azimuth angle between the subaperture images is too small, the target plane position offset is not sensitive to the target elevation, and the DEM extraction accuracy is low [22]. The size of the subaperture also needs to meet the azimuth resolution accuracy, where the azimuth resolution $\Delta\delta$ of the CSAR along the track direction on the data acquisition plane can be expressed as

$$\Delta\delta = \frac{c}{4f_c \sin(\phi/2)} \tag{6}$$

where $f_c$ is the signal center frequency, $\phi$ is the size of the subaperture, and $c$ is the speed of light.

The upper limit of the subaperture size can be defined by combining the correlation coefficient between the subapertures; the lower limit of the subaperture size can be defined by the accuracy requirements of the azimuth resolution. Select the appropriate subaperture size for division according to the above criteria.

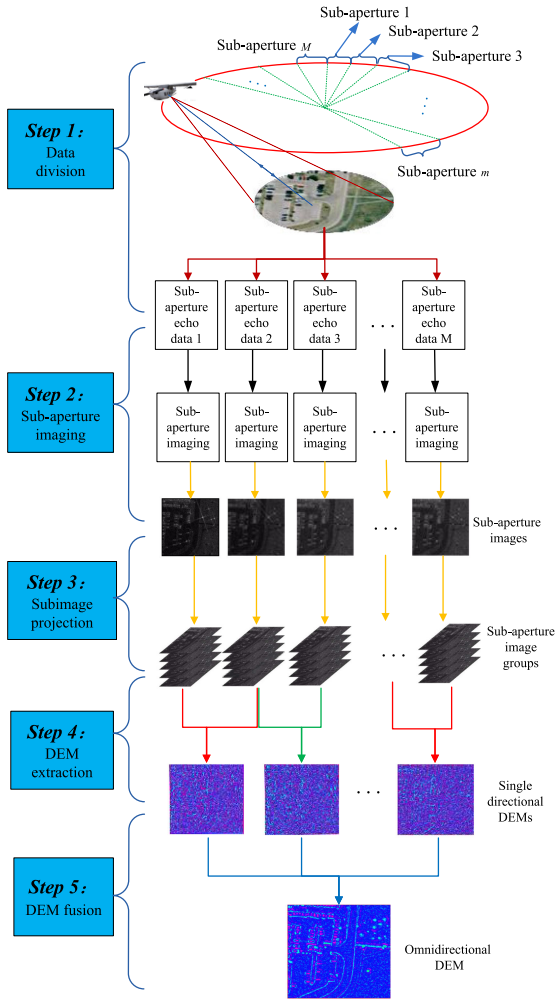


Fig. 3. Flowchart of DEM extraction by chain correlation method.

### B. Step 2: Subaperture Imaging

The BP algorithm is used to image the subaperture echo data. In order to improve the efficiency of the overall algorithm, we use the fast BP algorithm here, and use the computer GPU parallel operation to reduce the calculation time.

### C. Step 3: Subimage Projection

By projecting the subaperture data to the height direction, the influence of the geometric deformation changes between the CSAR subapertures on the correlation can be eliminated [25], as shown in Fig. 4. First, estimate the actual elevation range of the imaging target and the scene. Then according to the elevation range, a height coordinate axis is established, which is perpendicular to the 2-D imaging plane to form a 3-D space coordinate system. Finally, within the elevation range, the height values at equal intervals were taken as the imaging height. Each subaperture is imaged one by one according to different imaging heights and corresponds to the spatial coordinate system.

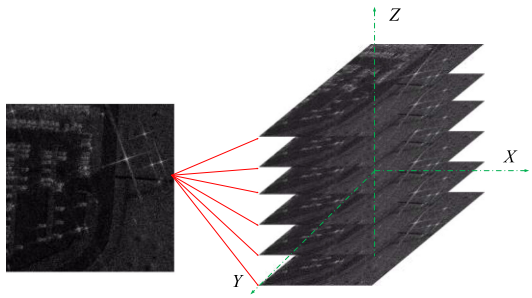


Fig. 4. Schematic diagram of height projection of subaperture data.

### D. Step 4: DEM Extraction

In the subaperture sequence, two adjacent subapertures are selected for normalized cross-correlation according to the corresponding imaging height, and chain correlation calculation is performed on the remaining subaperture images one by one to traverse all subapertures. The calculation formula for the correlation coefficient between subaperture images is as follows (7) shown at the bottom of this page, where $I_A$ and $I_B$ are the pixel amplitude values of the slider window in the two adjacent subaperture images $A$ and $B$ respectively, $\bar{I}_A$ and $\bar{I}_B$ are the average value of the pixel amplitude in the slider window, and let $K$ be the parameter to adjust the size of the slider, and the size of the slider is a square of $(2 \times K{+}1) \times (2 \times K{+}1)$ pixels. The center pixel in the slider window is the pixel to be estimated, and the surrounding pixels in the window are at the same height as the pixel to be estimated. The correlation coefficients between the subaperture images of each layer height are calculated according to the height axis direction, and the change of the correlation coefficient $\rho$ with the height axis is also calculated. Finally, the height value corresponding to the maximum correlation coefficient $\rho$ is selected as the true elevation of the position.

### E. Step 5: DEM Fusion

The correlation coefficients of two adjacent subapertures are calculated through chain correlation to obtain the corresponding DEM information. According to this method, the DEM information corresponding to all adjacent subapertures of the entire circumference is obtained, and the results are summed and averaged to get the all DEM information. The information is fused to obtain a full range of DEM, as shown in (8)

$$J = \frac{1}{N} \sum_{i=1}^{N} \rho_i \tag{8}$$

where $N$ is the number of the DEM information, and $J$ is the full range of DEM information.

In the traditional method, the circle data is divided into arcs and all the subaperture images in the arcs are used for joint correlation processing. The formula of the joint correlation coefficient of all subapertures in the arc is expressed as

$$JC(x, y, h) = \frac{\sum_{l=-L}^{L} \sum_{k=-K}^{K} \prod_{m=1}^{M} \left[ s_m(l,k) - \mu_m \right]}{\prod_{m=1}^{M} \sqrt{\sum_{l=-L}^{L} \sum_{k=-K}^{K} \left[ s_m(l,k) - \mu_m \right]^2}} \tag{9}$$

where $M$ is the number of subaperture images in the arc. The size of the slider is determined by the parameters $K$ and $L$ together, and the size of the slider is a rectangle of $(2 \times L{+}1) \times (2 \times K{+}1)$ pixels. $\mu_m$ is the average value of the pixel amplitudes in the slider window.

In the traditional method, the relevant information of all subaperture images in the arc are used, but from the Section II, the azimuth angle difference between the subaperture images is too large and the correlation between the subapertures is reduced. The accuracy of DEM information extraction is also affected. Moreover, the traditional method has a large amount of calculation due to the calculation of the correlation coefficients of all subapertures in the arc, and when the arc is divided, the arc overlaps mostly, which also causes a certain amount of repetition. This makes the running time of the whole algorithm too long.

Compared with traditional method, this article adopts the chain correlation method to calculate. After the subaperture size is reasonably divided, only the correlation between two adjacent subaperture images is calculated. The correlation between the images is higher, and the accuracy of the extracted DEM will be improved accordingly.

## IV. Experiment Results on Real Data

### A. X-Band CSAR DATA

In order to verify the effectiveness of the algorithm proposed in this article, this article selects the Gotcha experimental data publicly released by AFRL in 2006 for comparison and verification. The center frequency of the signal used by the radar system is 9.6 GHz and the bandwidth is 640 MHz. The field scene is treated as the experimental target.

According to the correlation between subapertures in the first section of the article, the width of each subaperture is set to 3°. At this time, the correlation between adjacent subapertures is strong, and it can meet the accuracy requirements of azimuth resolution. The entire circle data is divided into 120 subapertures, and focused imaging is performed through the BP algorithm. The grid spacing of imaging is 0.2 m, the height of the imaging

$$\rho = \frac{\sum_{i=-K}^{K} \sum_{j=-K}^{K} \left[ I_A(i,j) - \bar{I}_A \right] \left[ I_B(i,j) - \bar{I}_B \right]}{\sqrt{\sum_{i=-K}^{K} \sum_{j=-K}^{K} \left[ I_A(i,j) - \bar{I}_A \right]^2 \bullet \sum_{i=-K}^{K} \sum_{j=-K}^{K} \left[ I_B(i,j) - \bar{I}_B \right]^2}} \tag{7}$$

TABLE I
TARGET VEHICLE ELEVATION INFORMATION AND ESTIMATION RESULTS (UNIT/M)

| Car serial number | True height | Estimated mean elevation | | Root mean square error | |
|---|---|---|---|---|---|
| | | Chain correlation method | Joint correlation method | Chain correlation method | Joint correlation method |
| **A** | 1.43 | 1.3125 | 1.122 | 0.1086 | 0.809 |
| **B** | 1.41 | 1.3769 | 0.952 | 0.0823 | 0.930 |
| **C** | 1.47 | 1.3011 | 1.278 | 0.0583 | 0.780 |
| **D** | 1.41 | 1.4991 | 1.219 | 0.0893 | 0.889 |
| **E** | 1.44 | 1.4128 | 1.004 | 0.0865 | 1.036 |
| **F** | 1.67 | 1.5039 | 1.248 | 0.1024 | 0.765 |
| **G** | 1.36 | 1.4335 | 1.256 | 0.0738 | 0.818 |

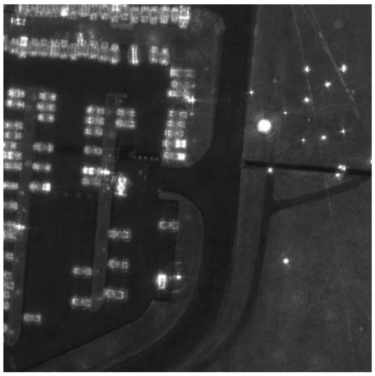

Fig. 5. CSAR full-aperture image of parking lot area in X-Band experimental scene.

TABLE II
COMPARISON ANALYSIS OF RESULTS

| Algorithm name | Mean of Elevation Error | Mean of the root mean square error | Time consuming |
|---|---|---|---|
| **Chain correlation method** | 0.0965m | 0.086m | 15267s |
| **Joint correlation method** | 0.3016m | 0.861m | 52441s |

plane is 0m, the imaging range is 100 × 100 m, and the CSAR 360° incoherent accumulation imaging results are shown in the Fig. 5.

When performing DEM extraction, select a slider window of 5 × 5 pixels to perform related calculations. The height-to-grid spacing is 0.2 m, and the elevation range is −1–3 m. The DEM extraction results of the chain correlation method and joint cross-correlation method are shown in Fig. 6. The DEM result diagram of the scene target vehicle extracted by the chain correlation method is shown in Fig. 7. It can be seen that the DEM information of the target scene extracted by the chain correlation method has a clear overall picture and low picture noise. It can clearly identify each part of the target scene information and can see the 3-D view of the target scene. The three-dimensional outline of the vehicle is more obvious.

Verify the seven target vehicles #A–#G in the scene. The number of each target vehicle follows the target number provided by Gotcha measured data. For facilitate viewing, the gray flat background represents the ground, the arrow direction is the head of the target vehicle. For the DEM extraction result of the target vehicle #F, comparing the two methods, the vehicle frame extracted by the chain correlation method is clearer, while the image of the vehicle extracted by the joint correlation method is relatively blurred.

Next, analyze the two methods from a quantitative perspective. Compare the average value and root mean square error of its height. Take the average height of the pixels on the roof of the target vehicle as the estimated height. The calculation formula of root mean square error is [28]

$$\sigma = \sqrt{\frac{1}{N}\sum_{n=1}^{N}\left(h_n - \bar{h}_n\right)^2} \tag{10}$$

where $N$ is the number of pixels used to evaluate the DEM information of the target vehicle; $h_n$ is the height value of the pixel$n$; $\bar{h}_n$ is the height average value of all pixels.

The processing results of the chain correlation method and the joint correlation method are shown in Table I. The result processing and comparison of the two methods are shown in Table II. The experimental results of the joint correlation method are obtained from [25].

Comparing the measured height of each vehicle with the real height, the measurement result of the method proposed in this article is closer to the real height. The mean of elevation error of the method proposed in this article is lower, indicating that the overall measurement result is more accurate. And the mean of the root mean square error of the method proposed in this article is lower which means the algorithm is more stable. The time consumption of the traditional algorithm is 52441 s, and for the algorithm in this article, it only needs 15267 s, which is only 29.11% of the original method.

### *B. Ku-Band CSAR DATA*

In order to further verify the applicability and accuracy of the algorithm proposed in this article, another experiment using

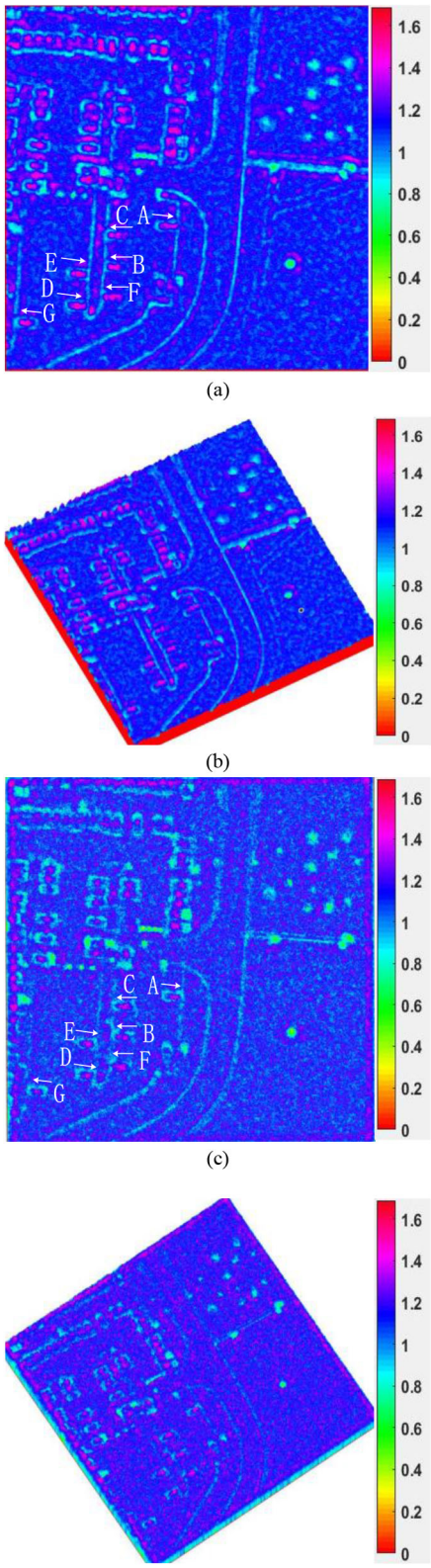


Fig. 6. DEM extraction results. (a) Top view of DEM extraction by chain correlation method (X-Band data). (b) Stereogram of DEM extraction by chain correlation method (X-Band data). (c) DEM extraction by joint cross-correlation method (X-Band data). (d) Stereogram of DEM extraction by chain correlation method (X-Band data).

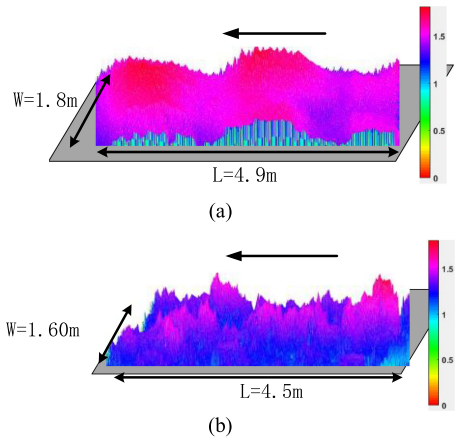


Fig. 7. DEM extraction results of target vehicle #F. (a) DEM extraction by chain correlation method. (b) DEM extraction by joint cross-correlation method.

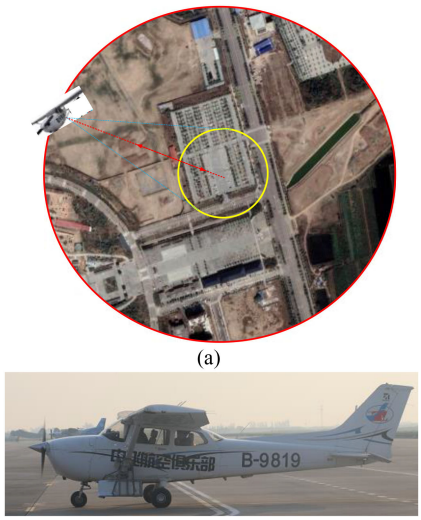


Fig. 8. Schematic diagram of the CSAR imaging scene. (a) Top view. (c) Experiment flight vehicle.

Ku-Band 360° omnidirectional circular-track SAR data is carried out. The real data are obtained by the Ku-Band SAR system independently developed by the National University of Defense Technology. The location is Shaanxi province, China. The incident angle of the antenna is 39°, and the spatial resolution is about 0.5 m. The schematic diagram of the CSAR imaging scene and experiment flight vehicle are shown in Fig. 8.

In order to select the appropriate subaperture width, according to the method proposed in theSection II of the article, the correlation coefficient between the subapertures is calculated as a function of the difference in azimuth angles. At the same time, considering that the azimuth resolution is higher than 0.2 m, the arc length of the subaperture is at least 3°. Two subaperture images are randomly selected for a certain azimuth angle difference, and their correlation coefficients are calculated in two ways: The whole image and pixel by pixel. The difference in azimuth angles between subapertures ranges from

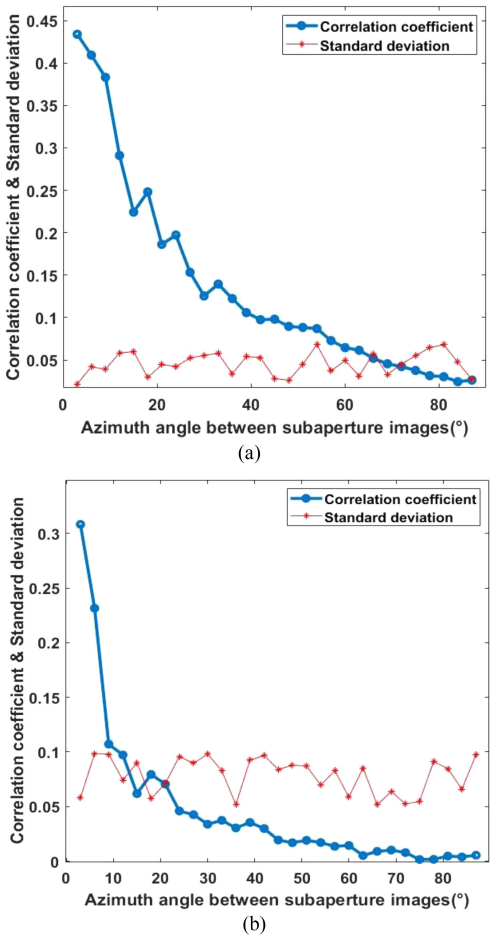


Fig. 9. Correlation between subaperture images varies with azimuth angle (blue line) and standard deviation of the results (red line). (a) Correlation between the entire subaperture images varies with the difference in azimuth angles. (b) Correlation between pixel-by-pixel subaperture images varies with azimuth angle difference.

3° to 87°. When calculating the correlation coefficient between subaperture images pixel by pixel, the size of the slider window for the correlation coefficient estimation is 21 × 21 pixels. For each difference in azimuth angles, also 10 pairs of subapertures are selected. Calculate the standard deviation of each group of experimental results and remove the bad data to reduce the error of the experiment. The average value of the image correlation coefficients of the 10 pairs of subapertures is used as the subaperture image correlation coefficient of the difference in azimuth angles. The result is shown in Fig. 9.

Through the above analysis, the subaperture azimuth width is set to 3°. In this setting, the correlation coefficient between adjacent subaperture images is the largest. The entire ring is divided into 120 subapertures, and the CSAR is imaged by 360° incoherent accumulation in all directions. In order to compare with the previous experimental data, the parking lot scene in the target area is selected as the experimental target for processing. The actual optical in the parking lot area is shown in Fig. 10. The range is 90 × 90 m, the imaging plane elevation is 0 m, the grid spacing is 0.15 m, and the image size is 601 × 601 pixels. The imaging result is shown in Fig. 11.

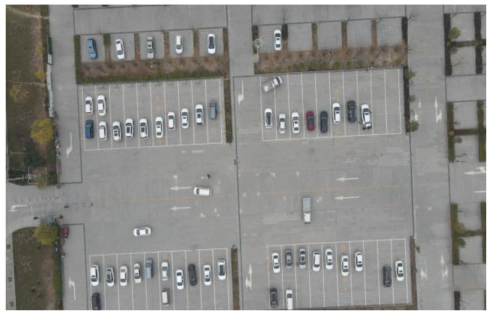

Fig. 10. Optical image of the parking lot area in the Ku-Band experimental scene.

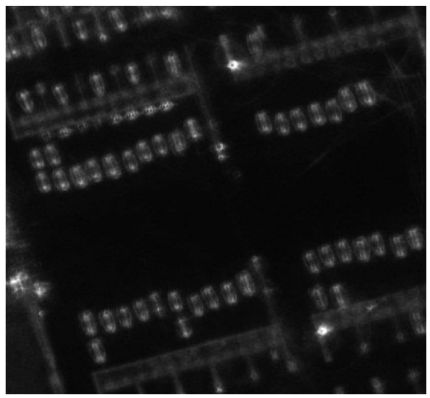

Fig. 11. Ku-Band experimental scene CSAR full-aperture image of parking lot area.

Perform DEM extraction according to the flowchart shown in Fig. 3, select a 5 × 5 pixel slider window for related calculations, the grid spacing of the height dimension is 0.2 m, and the height range is −1–3 m. The DEM extraction results by the two methods are shown in Fig. 12. The DEM extraction results of the target vehicle #B by the two methods are shown in Fig. 13.

From the comparison of DEM extraction results, it can be seen that the results of the joint correlation method in the literature [25] have a lot of noise in the overall picture, the outline of the target vehicle is not clear enough, and the main information loss of the vehicle is more serious. With the chain correlation method mentioned in this article, the overall result of the screen is clear, the target vehicle can be clearly identified, and the other parts of the screen are displayed intact. The stereo view is better, and the details are more abundant.

For the DEM extraction results of the target vehicle #B, comparing the two methods, the vehicle frame extracted by the chain correlation method is more complete, while the vehicle extracted by the joint correlation method has a relatively blurred picture and the loss of vehicle information is more serious.

Next, analyze the two methods from a quantitative perspective.

By comparing the four target vehicles #A–#D in the scene, the estimated height is compared with the actual height of the vehicle, and the root mean square error result of the estimated height of the vehicle is calculated [28]. The processing results of the chain correlation method and the joint correlation method

TABLE III
TARGET VEHICLE ELEVATION INFORMATION AND ESTIMATION RESULTS (UNIT/M)

| Car serial number | True height | Estimated mean elevation | | Root mean square error | |
|---|---|---|---|---|---|
| | | Chain correlation method | Joint correlation method | Chain correlation method | Joint correlation method |
| **A** | 1.488 | 1.4126 | 1.0192 | 0.1035 | 0.6163 |
| **B** | 1.460 | 1.3883 | 1.1213 | 0.1091 | 0.6437 |
| **C** | 1.454 | 1.4254 | 1.0444 | 0.0851 | 0.8221 |
| **D** | 1.474 | 1.4565 | 1.1302 | 0.1176 | 0.6445 |

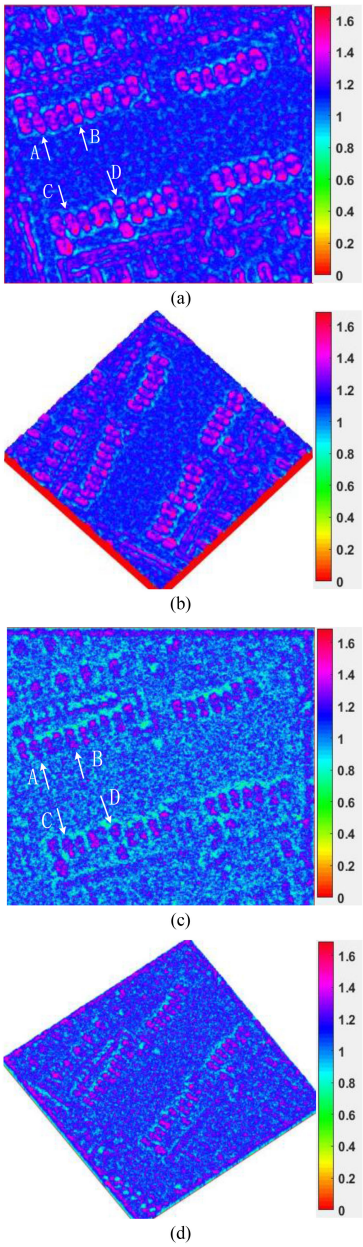


Fig. 12. DEM extraction results. (a) Top view of DEM extraction by chain correlation method (Ku-Band data). (b) Stereogram of DEM extraction by chain correlation method (Ku-Band data). (c) DEM extraction by joint cross-correlation method (Ku-Band data). (d) Stereogram of DEM extraction by joint cross-correlation method (Ku-Band data).

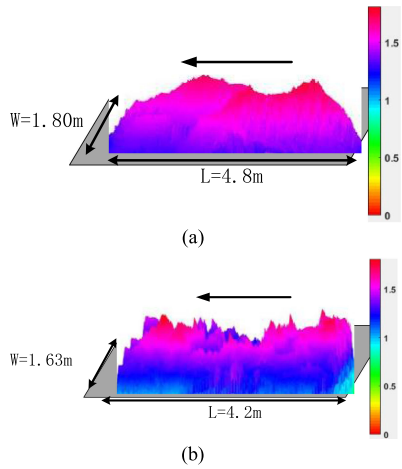


Fig. 13. DEM extraction results of target vehicle #B. (a) DEM extraction by chain correlation method. (b) DEM extraction by joint cross-correlation method.

TABLE IV
COMPARISON ANALYSIS OF RESULTS

| Algorithm name | Mean of Elevation Error | Mean of the root mean square error | Time consuming |
|---|---|---|---|
| **Chain correlation method** | 0.0483m | 0.1038m | 10376s |
| **Joint correlation method** | 0.3902m | 0.6817m | 40057s |

are shown in Table III. The result processing and comparison of the two methods are shown in Table IV.

Comparing the measured height of each vehicle with the real height, the measurement result of the method proposed in this article is closer to the real height. The mean of elevation error of the method proposed in this article is lower, and the error range of the average height is between 0.02 and 0.08 m, indicating that the overall measurement result is more accurate. And the mean of the root mean square error of the method proposed in this article is lower which means the algorithm is more stable. The time consumption of the traditional algorithm is 40 057 s, and for the algorithm in this article, it only needs 10 376 s, which is only 25.90% of the original method.

In the verification of the real data in the two frequency bands, the calculation results of the method proposed in this article

are better than the original method, whether qualitatively or quantitatively.

## V. Conclusion

By observing the correlation between CSAR subaperture images, this article proposes a method to extract the DEM information of the target area by using CSAR 360° full-aperture images. This method extracts the target scene DEM by using the strong correlation between adjacent subaperture images, and traverses the entire circle in the manner of adjacent subapertures, which improves the stability of the algorithm and improves the accuracy of DEM extraction. The method can draw a three-dimensional view of the target scene.

Finally, the method is tested with the real data, and the effectiveness and accuracy of the algorithm in this article are verified by comparative analysis of the results, and the applicability of the method is verified by verifying different experimental data.

However, when performing 3D reconstruction, we have not considered the impact of image noise. Regarding the denoising preprocessing of a single frame of SAR image, combined with the latest research content on neural networks and deep learning [29]–[31], the influence of single frame SAR noise can be effectively removed, which will be of great help to the improvement of our extraction results.

## Acknowledgment

The authors would like to thank the reviewers for their very competent comments and helpful suggestions that helped to improve this article.

## References

[1] A. Ishimaru, T. K. Chan, and Y. Kuga, "An imaging technique using confocal circular synthetic aperture radar," *IEEE Trans. Geosci. Remote Sens.*, vol. 36, no. 5, pp. 1524–1530, Sep. 1998.

[2] F. Banda and S. Tebaldini, "Texture-free absolute DEM retrieval from opposite-side multi-baseline InSAR data," in *Proc. IEEE Int. Geosci. Remote Sens. Symp.*, 2015, pp. 4085–4088.

[3] H. Rudolf, D. Tarchi, and A. J. Sieber, "Combination of linear and circular SAR for 3-D features," in *Proc. IEEE Int. Geosci. Remote Sens. Symp. Proc. Remote Sens.–Sci. Vis. Sustain. Develop.*, vol. 4, 1997, pp. 1551–1553.

[4] M. Soumekh, "Reconnaissance with slant plane circular SAR imaging," *IEEE Trans. Image Process.*, vol. 5, no. 8, pp. 1252–1265, Aug. 1996.

[5] M. Y. Jin and M. Chen, "Analysis and simulation for a spotlight-mode aircraft SAR in circular flight path," in *Proc. IEEE Int. Geosci. Remote Sens. Symp.*, 1993, pp. 1777–1780.

[6] Z. S. Wang, Z. Q. Wang, and J. Xu, "The effect of orientation of circular orbiting space-borne SAR on image reconstruction," in *Proc IEEE Int. Geosci. Remote Sens. Symp.*, 1993, pp. 794–795.

[7] M. S. Seymour and I. G. Cumming, "Maximum likelihood estimation for SAR interferometry," in *Proc. IEEE Int. Geosci. Remote Sens. Symp.*, 1994, pp. 2272–2275.

[8] T. K. Chan, Y. Kuga, and A. Ishimaru, "Feasibility study on localized subsurface imaging using circular synthetic aperture radar and angular correlation function measurement," in *Proc. IEEE Int. Geosci. Remote Sens. Symp. Proc. Remote Sens. – Sci. Vis. Sustain. Develop.*, 1997, pp. 1138–1140.

[9] J. W. Bredow, R. L. Porco, and G. Hartman, "Circular and linear polarization inverse SAR imaging of simple deterministic targets and statistically known randomly rough surfaces using constant and varying illumination," in *Proc. Int. Geosci. Remote Sens. Symp.*, 1992, pp. 1193–1194.

[10] T. K. Chan, Y. Kuga, and A. Ishimaru, "Experimental studies on circular SAR imaging in clutter using angular correlation function technique," *IEEE Trans. Geosci. Remote Sens.,* vol. 37, no. 5, pp. 2192–2197, Sep. 1999.

[11] W. Hong, "Progress in circular SAR imaging technique," *J. Radars*, vol. 1, no. 2, pp. 124–135, Jun. 2012.

[12] L. Chen, D. An, and X. Huang, "A backprojetion-based imaging for circular synthetic aperture radar," *IEEE J. Sel. Topics Appl. Earth Observ. Remote Sens.,* vol. 10, no. 8, pp. 3547–3555, Aug. 2017.

[13] Y. Lin, W. Hong, W. Tan, Y. Wang, and M. Xiang, "Airborne circular SAR imaging: Results at P-band," in *Proc. IEEE Int. Geosci. Remote Sens. Symp.*, 2012, pp. 5594–5597.

[14] L. Yan, W. Yuan, S. Guang-cai, and X. Meng-dao, "Fast imaging processing of circular SAR," *J. Electron. Inf. Technol.*, vol. 35, no. 4, pp. 852–858, Apr. 2013.

[15] W. Wu, H. Guo, X. Li, L. Ferro-Famil, and L. Zhang, "Urban land use information extraction using the ultrahigh-resolution chinese airborne SAR imagery," *IEEE Trans. Geosci. Remote Sens.*, vol. 53, no. 10, pp. 5583–5599, Oct. 2015.

[16] H. Oriot and H. Cantalloube, "Circular SAR imagery for urban remote sensing," in *Proc. 7th Eur. Conf. Synthetic Aperture Radar*, 2008, pp. 1–4.

[17] S. Palm and H. Oriot, "DEM extraction over urban area using circular SAR imagery," in *Proc. 8th Eur. Conf. Synthetic Aperture Radar*, Aachen, Germany, 2010, pp. 1–4.

[18] O. Ponce *et al.*, "Fully polarimetric high-resolution 3-D imaging with circular SAR at L-band," *IEEE Trans. Geosci. Remote Sens.*, vol. 52, no. 6, pp. 3074–3090, Jun. 2014.

[19] O. Ponce, P. Prats, R. Scheiber, A. Reigber, I. Hajnsek, and A. Moreira, "Polarimetric 3-D imaging with airborne holographic SAR tomography over glaciers," in *Proc. IEEE Int. Geosci. Remote Sens. Symp.*, 2015, pp. 5280–5283.

[20] O. Ponce, P. Prats-Iraola, R. Scheiber, A. Reigber, A. Moreira, and E. Aguilera, "Polarimetric 3-D reconstruction from multicircular SAR at P-Band," *IEEE Geosci. Remote Sens. Lett.,* vol. 11, no. 4, pp. 803–807, Apr. 2014.

[21] O. Ponce, P. Prats, R. Scheiber, A. Reigber, and A. Moreira, "First demonstration of 3-D holographic tomography with fully polarimetric multi-circular SAR at L-band," in *Proc. IEEE Int. Geosci. Remote Sens. Symp.*, 2013, pp. 1127–1130.

[22] L. Ting, L. Yun, T. Wei-xian, H. Wen, and W. Yan-Ping, "DEM extraction over urban area using circular SAR imagery," *J. Graduate Univ. Chin. Acad. Sci.*, vol. 30, no. 1, pp. 47–52, 2013.

[23] S. Demirci, E. Yigit, and C. Ozdemir, "Wide-field circular SAR imaging: An empirical assessment of layover effects," *Microw. Opt. Technol. Lett.*, vol. 57, no. 2, pp. 489–497, Feb. 2015.

[24] L. P. Chen, D. X. AN, and X. T. Huang, "Resolution analysis of circular synthetic aperture radar noncoherent imaging," *IEEE Trans. Instrum. Meas.*, vol. 69, no. 1, pp. 231–240, Jan. 2020.

[25] Z. Jin-qiang, S. Zhi-yong, L. Zhen-fang, and B. Zheng, "Joint cross-correlation DEM extraction method for CSAR subaperture image sequences," *Syst. Eng. Electron.*, vol. 40, no. 9, pp. 1939–1944, 2018.

[26] S. Palm, R. Sommer, D. Janssen, A. Tessmann, and U. Stilla, "Airborne circular W-band SAR for multiple aspect urban site monitoring," *IEEE Trans. Geosci. Remote Sens.,* vol. 57, no. 9, pp. 6996–7016, Sep. 2019.

[27] S. Palm and U. Stilla, "3-D point cloud generation from airborne single-pass and single-channel circular SAR data," *IEEE Trans. Geosci. Remote Sens.*, to be published, doi: 10.1109/TGRS.2020.3041320.

[28] T. Yang, Z. Li, Y. Liu, Z. Suo, and Z. Bao, "Channel error estimation methods for multi-channel HRWSSAR systems," in *Proc. IEEE Int. Geosci. Remote Sens. Symp.*, 2013, pp. 4507–4510.

[29] F. Samadi, G. Akbarizadeh, and H. Kaabi, "Change detection in SAR images using deep belief network: A new training approach based on morphological images," *IET Image Process.*, vol. 13, no. 12, pp. 2255–2264, May 2019.

[30] M. Zalpour, G. Akbarizadeh, and N. Alaei-Sheini, "A new approach for oil tank detection using deep learning features with control false alarm rate in high-resolution satellite imagery," *Int. J. Remote Sens.,* vol. 41, no. 6, pp. 2239–2262, 2020.

[31] N. Davari, G. Akbarizadeh, and E. Mashhour, "Intelligent diagnosis of incipient fault in power distribution lines based on corona detection in UV-visible videos," *IEEE Trans. Power Del.*, to be published, doi: 10.1109/TPWRD.2020.3046161.

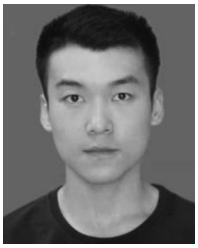

**Yishi Li** received the undergraduate degree in electronic information engineering from the Xidian University, Xi'an, China, in 2019. He is currently working toward the postgraduate degree in information and communication engineering with the National University of Defense Technology, Changsha, China.

His research interests include signal processing and circular synthetic aperture radar (CSAR) image formation.

**Leping Chen** received the B.S. degree in electronic engineering, and the M.S. and Ph.D. degrees in information and communication engineering from the National University of Defense Technology, Changsha, China, in 2011, 2014, and 2018, respectively.

He is currently a Lecturer with the National University of Defense Technology. His research interests include circular synthetic aperture radar (CSAR) image formation and high resolution SAR image formation.

**Daoxiang An** received the B.S., M.S., and Ph.D. degrees in information and communication engineering from the National University of Defense Technology, Changsha, China, in 2004, 2006, and 2011, respectively.

He is currently an Associate Professor with the National University of Defense Technology. His research interests include ultrawideband SAR, circular SAR, SAR interferometry, SAR-GMTI, radar system development, and deep learning in SAR images.

**Zhimin Zhou** received the B.S. degree in aeronautical radio measurement and control, and the M.S. and Ph.D. degrees in information and communication engineering from the National University of Defense Technology (NUDT), Changsha, China, in 1982, 1989, and 2002, respectively.

He is currently a Professor with NUDT. His research interests include ultrawideband radar system and real-time signal processing.

Dr. Zhou is a Fellow of the Chinese Institute of Electronics.